



Crustal structure beneath the Ethiopian Plateau and adjacent areas from receiver functions: Implications for partial melting and magmatic underplating

Tuo Wang, Stephen S. Gao, Qiuyue Yang, Kelly H. Liu^{*}

Geology and Geophysics Program, Missouri University of Science and Technology, Rolla, MO 65409, USA

ARTICLE INFO

Keywords:

Crustal structure
Ethiopian Plateau
Receiver function

ABSTRACT

Receiver function measurements of crustal thickness (H) and Vp/Vs provide important information on the formation and evolution of continental plateaus and rift zones such as the Ethiopian Plateau, the Afar and Main Ethiopian Rifts in northeastern Africa. Unfortunately, the presence of a low-velocity sedimentary layer atop most of the Cenozoic rift basins may lead to strong reverberations that can mask the P-to-S conversions from the Moho, resulting in unreliable H and Vp/Vs measurements. Here we estimate H and Vp/Vs beneath the Afar Depression (AD), Ethiopian Plateau (EP), and the Main Ethiopian Rift (MER) by stacking receiver functions. Reliable H and Vp/Vs measurements are obtained at a total of 69 stations, among which 18 stations are pre-processed by applying the reverberation removal technique. In comparison to the MER and EP, the AD is characterized by a thinner crust and higher Vp/Vs, and the thinnest crust and highest Vp/Vs are found in the Red Sea Rift (RSR) in central AD. Gradual variations of H and Vp/Vs between the previous and present axes of the RSR support a gradual rather than jumpy migration model of the axis. The overall high Vp/Vs values in the study area can be interpreted as a combined result of continental flood basalts at the surface, magmatic intrusion, and crustal partial melting. The relatively low amplitude of the P-to-S converted phases from the Moho observed in the southern part of the western Ethiopian Plateau and the AD with the exception of the RSR may be attributed to magmatic underplating.

1. Introduction

1.1. Geological setting

The Afar Depression (AD) in northeast Africa (Fig. 1) is the most developed section of the East African Rift System (EARS). The Red Sea Rift (RSR), Gulf of Aden Rift (GAR), and the Main Ethiopian Rift (MER) meet in the AD to form a rift-rift-rift triple junction with the Arabian Plate to the northeast, the Nubian Plate to the west, and the Somalian Plate to the southeast (Hofmann et al., 1997; McKenzie et al., 1970). The MER separates the Ethiopian Plateau (EP), a 1000 km wide Palaeogene flood basalt province with an average elevation of ~2.5 km (Mohr and Zanettin, 1988), into the western Ethiopian Plateau (WEP) to its northwest and the eastern Ethiopian Plateau (EEP) to its southeast.

In central Afar, the Tendaho graben-Goba'ad graben region is widely regarded as the Afar triple junction, even though the arm of the GAR propagated landward farther to the north and failed to meet with the

other two active arms of the rift system (Courtilot et al., 1987; Manighetti et al., 1997; Manighetti et al., 1998; Tesfaye et al., 2003). The earliest known rifting in the AD occurred at ~35 Ma (d'Acremont et al., 2005; Davidson and Rex, 1980; Ebinger et al., 1993). Rifting has progressed to seafloor spreading in the Gulf of Aden, where seafloor spreading initiated at ~16.5 Ma (e.g., d'Acremont et al., 2005), and propagated westward into the AD by ~0.7 Ma (Audin et al., 2001). Magnetic anomalies of the Aden ridge are observed inland as far as the Tendaho Graben-Goba'ad Graben region, suggesting either complex history of ridge jumps (Courtilot et al., 1984) or an extremely asymmetric spreading (Barberi and Varet, 1977). Extension in the southernmost RSR initiated between 29 and 26 Ma, and was at ~10°N until the linkage of the MER and southern Red Sea occurred at ~10 Ma (Wolfenden et al., 2005). The rifting-related SSE-trending spreading ridge propagated along the Gulf of Zula to the northwest of the AD, and stepped onto land within the Danakil Depression (Chu and Gordon, 1998). Continuously propagating southward along the Erta Ale axial

^{*} Corresponding author.

E-mail address: liukh@mst.edu (K.H. Liu).

<https://doi.org/10.1016/j.tecto.2021.228857>

Received 8 May 2020; Received in revised form 24 August 2020; Accepted 22 March 2021

Available online 31 March 2021

0040-1951/© 2021 Elsevier B.V. All rights reserved.

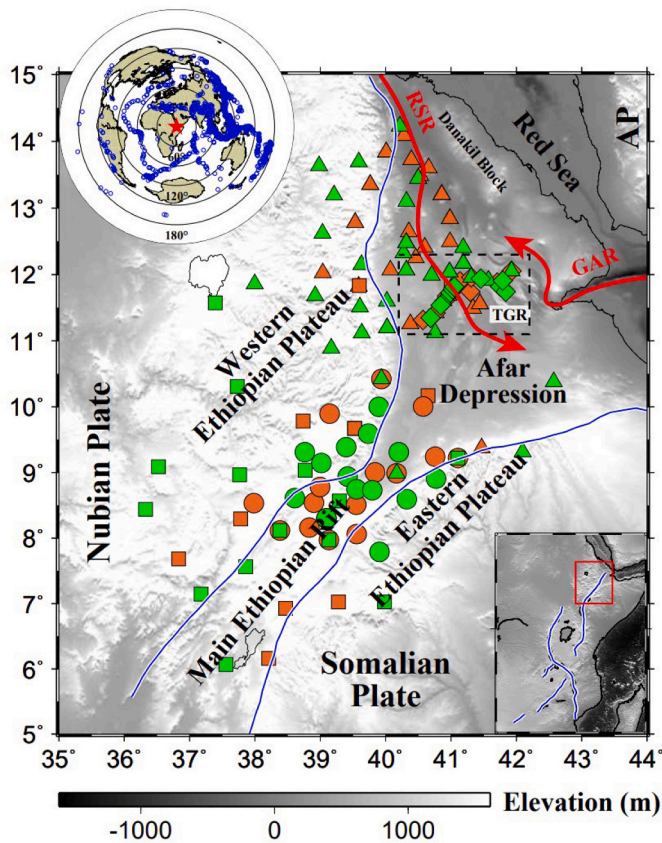


Fig. 1. A topographic map of the study area showing major tectonic provinces and seismic stations used in the study. The blue lines define the boundaries of the EARS. The two red curves with arrows represent the Red Sea Rift (RSR) and Gulf of Aden Rift (GAR), respectively, and the arrows show the propagation directions of the spreading ridges. The Tendaho graben-Goba'ad graben (TGR) region is outlined by the dashed rectangle. Diamonds represent stations from the ALIE project, triangles for the AFAR project, circles for the EAGLE project, and squares for the EBSE project. Stations represented by orange symbols did not result in reliable results from this study. The inset in the upper left corner is an azimuthal equidistant projection map centered at the study area showing the distribution of earthquakes (blue circles) used in the study. The rectangle area in the inset map at the lower right corner shows the location of the study area. AP: Arabian Plate; GAR: Gulf of Aden Rift; RSR: Red Sea Rift; TGR: Tendaho graben-Goba'ad graben. (For interpretation of the references to colour in this figure legend, the reader is referred to the web version of this article.)

volcanic ranges, the spreading ridge terminates in central Afar (Beyene and Abdelsalam, 2005). Initiation of the ESE-directed extension of the MER between the Nubian and Somalian plates occurred at ~ 18 Ma (WoldeGabriel et al., 1990), and the extension propagated northward into the present-day Afar triple junction at $\sim 10^\circ$ N at ~ 11 Ma (Tesfaye et al., 2003; Wolfenden et al., 2004 and 2005). The northern part of the MER is characterized by magmatic rift segments that are commonly ~ 20 km in width and ~ 60 km in length (Ebinger and Casey, 2001). Due to the variation in lithosphere thickness and magma supply, the size of magmatic rift segments systematically decreased northeastward to central Afar (Hayward and Ebinger, 1996).

The RSR is characterized by the transition between continental rifting of the EARS and seafloor spreading in the Red Sea and Gulf of Aden (Bastow and Keir, 2011; Makris and Ginzburg, 1987). The region is associated with the Eocene-Oligocene flood basalt province lying atop the EP (Wolfenden et al., 2005). Currently, the Arabian Plate is moving away from the Nubian Plate at a rate of ~ 1.6 cm/yr (Chu and Gordon, 1998). The motion of the Arabian Plate caused the formation of the Red Sea between the Nubian and Arabian plates and led to the opening of the

Gulf of Aden between the Somalian and Arabian plates (Tesfaye et al., 2003). Investigation of the crustal structure and seismic properties at the AD could provide insights into crustal modification by stretching and magmatic intrusion, and shed light on the processes responsible for the transition from continental rifting to the formation of oceanic crust, a process that is believed to be happening along the RSR (Bridges et al., 2012; Makris and Ginzburg, 1987).

1.2. Results from previous studies of crustal structure

1.2.1. Receiver function studies

Dugda et al. (2005) conducted a receiver function (RF) study in Ethiopia and Kenya. Data from 27 seismic stations (green symbols in Fig. 2) within or adjacent to the MER, mainly from the Ethiopia Broadband Seismic Experiment (EBSE) project (Nyblade and Langston, 2002), were applied to measure the crustal thickness (H) and V_p/V_s . Within the MER, the resulting H values vary from 27 to 38 km, and the resulting V_p/V_s values vary from 1.80 to 2.21. The H measurements show a general increase and the V_p/V_s measurements demonstrate an approximate decrease toward the rift shoulders from the central part of the MER. Beneath the WEP and EEP adjacent to the MER, the H measurements range from 33 to 44 km, and the V_p/V_s measurements range from 1.66 to 1.84. For the single station (Station TEND) in the AD, the measured H and V_p/V_s are 25 km and 2.16, respectively (Fig. 2). The high V_p/V_s in the AD is possibly caused by the mafic crust and partial melt, which is also supported by Ruegg (1975).

Using seismic stations mainly from the Ethiopia-Afar Geoscientific Lithospheric Experiment (EAGLE) project (Maguire et al., 2003), Stuart et al. (2006) obtained crustal structure in the MER based on RF analyses at 40 stations (red symbols in Fig. 2). Within the rift, the observed H ranges from 30 km at the northern part to 38 km at the southern part of the rift zone. On the WEP, the H of 41 to 43 km was observed on the NW part, which is thicker than that observed on the SW part (~ 36 km). These observations are consistent with results from the receiver function study of Ayele et al. (2004), which obtained an H value of ~ 40 km beneath two seismic stations in the central WEP. The resulting V_p/V_s measurements within the MER increase to greater than 2.0 northward to the triple-junction region. Outside the MER, the averaged V_p/V_s value on the WEP (~ 1.85) is slightly greater than that on the EEP (~ 1.80), which was interpreted as either the result of magmatic activity or the difference in the pre-rift crustal compositions.

Hammond et al. (2011) utilized H- V_p/V_s stacking analysis to image crustal structure beneath the AD, the northern portion of the MER, and the adjacent areas of the EP, using data from 48 stations (orange symbols in Fig. 2) mainly from the multinational collaborative Afar Consortium (AFAR) project. The thickest crust of 45 km is found beneath the WEP, while the thinnest crust of 16 km is observed beneath the incipient oceanic spreading center at the northern part of the triple junction in the AD. They also obtained H of 20–26 km outside the currently active rift zones. The WEP shows crust with V_p/V_s values varying between 1.7 and 1.9. Within the rift, the observed V_p/V_s values are mostly greater than 2.0 beneath the current axis of the RSR, which are higher than those beneath the eastern part of the AD (less than 1.9) and are suggestive of a higher degree of partial melt.

Using RFs recorded by 20 stations (purple symbols in Fig. 2) mainly from the Afar Lithosphere Imaging Experiment (ALIE), Reed et al. (2014) obtained high-resolution images of the crust beneath the southeastern end of the RSR in the central part of the triple-junction area. The resulting H measurements range from ~ 17 km near the RSR axis to ~ 30 km at the overlap region of the RSR and GAR, with an average value of 22 ± 4 km. High V_p/V_s values (greater than 2.0) were observed at most of the stations, which are indicative of pervasive melting in the crust (Reed et al., 2014).

A recent P-wave receiver function study (Kibret et al., 2019) revealed crustal structure beneath four seismic stations (blue symbols in Fig. 2a) using high quality seismic data. Moho depth beneath the station in the

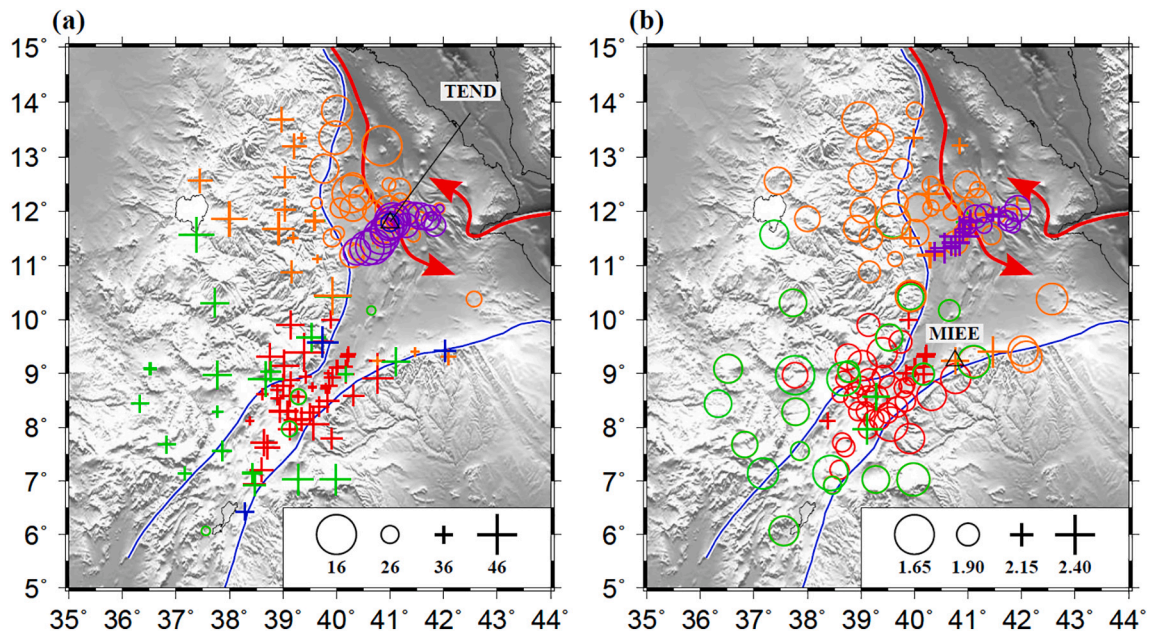


Fig. 2. (a) Previous H measurements. The open triangle represents Station TEND that is discussed in the main text. (b) Previous Vp/Vs measurements. The open triangle represents Station MIEE. Green symbols represent measurements from [Dugda et al. \(2005\)](#), red ones from [Stuart et al. \(2006\)](#), orange ones from [Hammond et al. \(2011\)](#), purple ones from [Reed et al. \(2014\)](#), and blue ones from [Kibret et al. \(2019\)](#). See [Fig. 1](#) for explanations of the blue lines and red curves. (For interpretation of the references to colour in this figure legend, the reader is referred to the web version of this article.)

western AD is 26 ± 2 km, and a low velocity gradient found at the depth of ~ 16 km beneath the station may suggest the existence of crustal partial melt. The other three stations are located along the boundary zone between the EP and MER or AD, where greater crustal thickness values ranging from 36 to 42 km were reported, which are generally in agreement with previous observations at the same or nearby stations.

1.2.2. Wide-angle and seismic tomography studies

[Makris and Ginzburg \(1987\)](#) used seismic refraction data acquired along six profiles to investigate the northern MER and the Afar triple junction, and observed an ~ 3 km thick sedimentary layer with P wave velocity of ~ 3.35 km/s and a basalt layer with an average P wave velocity of ~ 4.5 km/s extending to the depth of ~ 6 km toward the axis of the RSR. Within the northern MER, from SW to NE, the resulting H ranges from 30 to 26 km, and in the triple junction region, the H measurements, varying from 14 to 26 km, gradually decrease toward the Red Sea.

Using active-source seismic reflection/refraction profile across the MER, [Mackenzie et al. \(2005\)](#) observed a 2- to 5-km-thick sedimentary cover beneath the profile, along which the thickest sedimentary cover of ~ 5 km with P wave velocity of ~ 3.3 km/s was found beneath two of the four magmatic segments within the MER. H varies from ~ 33 km at the WEP to ~ 30 km at the axis of the MER, and increases toward the EEP reaching to ~ 36 km. Using the same data set used by [Mackenzie et al. \(2005\)](#), [Maguire et al. \(2006\)](#) interpreted crustal structure along a rift parallel and a rift orthogonal profile. The crust thins from ~ 36 km at the SW part of the profile to ~ 25 km at the NE part. A 2- to 5-km-thick sedimentary cover was observed beneath the rift-axial profile with an average P wave velocity of 4.2 km/s. The existence of sediments in the upper crust is also supported by other tomographic studies (e.g., [Keranen et al., 2009](#); [Kim et al., 2012](#)).

[Dugda et al. \(2007\)](#) conducted a joint inversion of surface wave group velocities and receiver functions to investigate velocity structure beneath the MER and the southern Afar. The resulting S wave velocity model shows H beneath the EP ranging from 35 to 44 km, which thins to 25 to 35 km in the MER and southern AD. The surface wave tomography study conducted by [Guidarelli et al. \(2011\)](#) obtained group velocity

maps at the periods between 5 and 25 s. A significant low velocity anomaly (about -20%) was observed beneath the sites of recent dyke intrusions at the Dabbahu and Manda-Hararo magmatic segments in the AD, indicating the presence of unconsolidated sediments. S wave velocities were inverted within an active magmatic segment, and a low velocity zone ($V_s \sim 3.2$ km/s) between the depth of 6 and 12 km was revealed in the crust, suggesting the presence of partial melt in the lower crust.

A recent ambient seismic noise tomography study by [Chambers et al. \(2019\)](#) imaged a well-constrained 3-D absolute shear wave velocity model from the surface to the depth of 60 km in the northern part of the EARS. 170 seismic stations were utilized to provide ambient seismic noise data. The inferred H values vary from 40 km in the MER to 20 km in the AD. Along the SW-NE trending cross section, the thinnest crust of 17 km was found beneath the Red Sea, while the crust thickens to 29 km beneath Yemen on the Arabian Plate. The slowest crustal velocities observed in the MER are in agreement with the longer magma residence times. Besides, low velocities in the uppermost mantle beneath almost the entire study region indicated the pervasive existence of partial melt.

1.3. Goals and significance of the present study

As demonstrated in [Fig. 2](#), none of the previous studies covered all the four tectonic provinces (AD, MER, EEP, and WEP), preventing a direct comparison of crustal characteristics among the provinces. Additionally, significant discrepancies exist in the resulting H and especially the Vp/Vs measurements obtained at the same stations, i.e., for Station MIEE in the northeastern MER, [Hammond et al. \(2011\)](#) measured H to be 32 km and Vp/Vs to be 2.22, while [Stuart et al. \(2006\)](#) estimated the H to be 35 km and the Vp/Vs to be 2.09 ([Fig. 2](#)). Such discrepancies may have originated from the different data processing parameters used in different studies, including the filtering frequencies, criteria for selecting RFs, as well as the reference mean crustal velocity. The discrepancies are the largest at stations in the AD and MER, where the presence of a low velocity sedimentary layer has been reported ([Guidarelli et al., 2011](#)). The bottom of the low velocity layer and the free surface can produce strong reverberations that mask the converted

phases from the Moho (Yu et al., 2015; Zelt and Ellis, 1999). To our knowledge, none of the previous RF studies (Fig. 2) in this region attempted to remove the reverberations, which may lead to erroneous H and Vp/Vs measurements. In this study, we utilize a deconvolution-based reverberation-removal technique (Yu et al., 2015) to remove the effects of the low-velocity sedimentary layer at a significant portion of the stations, and systematically measure H and Vp/Vs in all the four tectonic provinces in NE Africa.

2. Data and methods

2.1. Data

The three-component broadband teleseismic data used in the study were recorded by 140 seismic stations belonging to 4 projects, including the Ethiopia Broadband Seismic Experiment (EBSE; Dugda et al., 2005; Nyblade and Langston, 2002), Ethiopia-Afar Geoscientific Lithospheric Experiment (EAGLE; Stuart et al., 2006), multinational collaborative

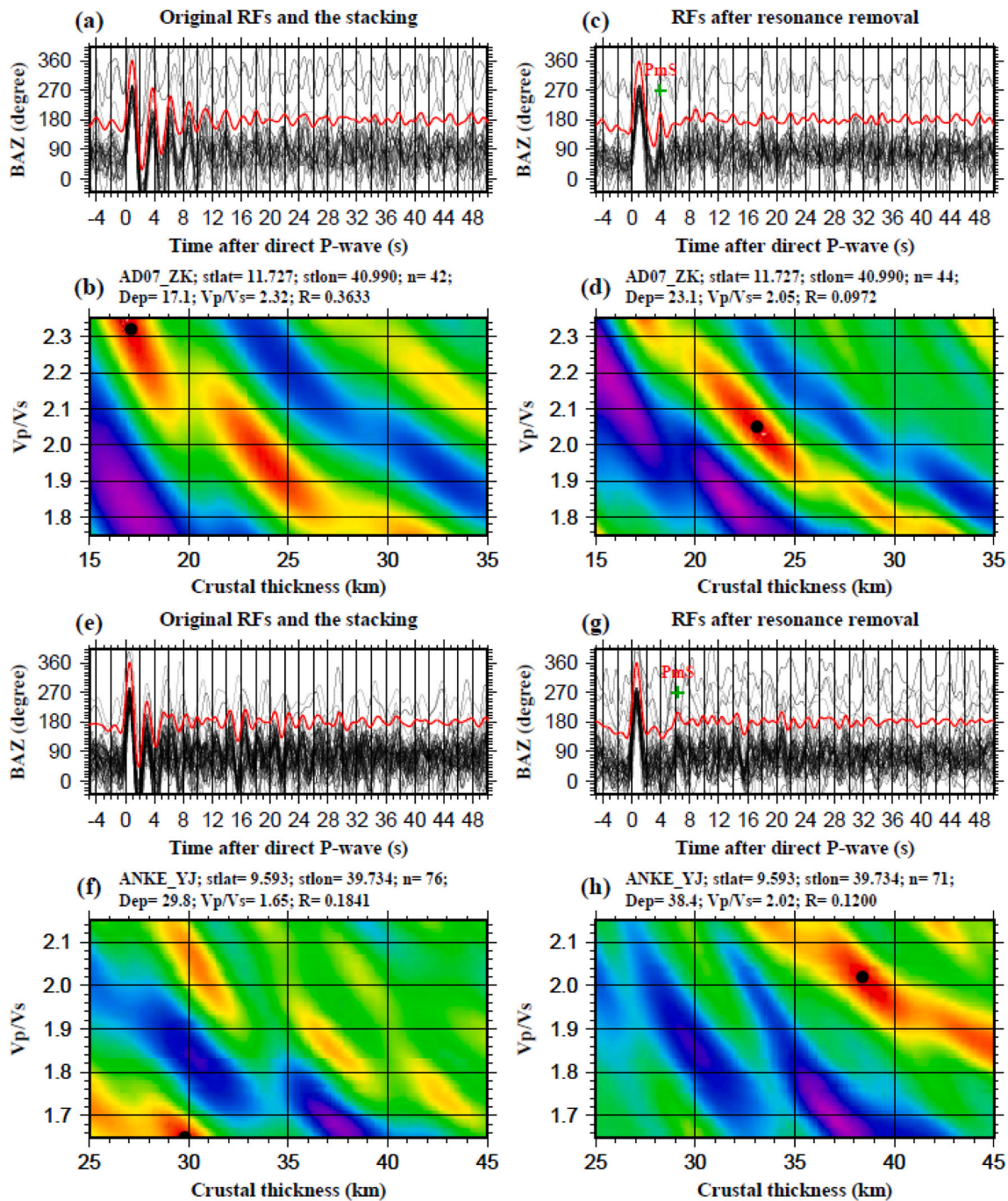


Fig. 3. (a) Original RFs from Station AD07 (see Fig. 4 for the location of this station) plotted against back azimuth. The red trace is the result of simple time domain summation of the individual RFs and demonstrates strong reverberations. (b) H-Vp/Vs stacking using the original (i.e., pre-reverberation removal) RFs shown in (a). The black dot denotes the maximum stacking amplitude, “n” represents the number of RFs, and “R” represents the maximum stacking amplitude. (c) Same as (a) but for RFs after removing the reverberations using the approach of Yu et al. (2015). The green cross indicates the location of the PmS. (d) H-Vp/Vs stacking using reverberation-removed RFs shown in (c). (e) - (h) are the same as (a) - (d), respectively, but for Station ANKE. (For interpretation of the references to colour in this figure legend, the reader is referred to the web version of this article.)

Afar Consortium (AFAR; Hammond et al., 2011), and the Afar Lithosphere Imaging Experiment (ALIE; Reed et al., 2014), within the area of 35°E - 44°E and 5°N - 15°N (Fig. 1). The entire data set has been archived at the Incorporated Research Institutions for Seismology (IRIS) Data Management Center (DMC) and is publicly accessible.

The seismic data requested were from earthquakes in the epicentral distance range of 30° to 180° occurred over the period of January 2000 to December 2018, with a cutoff magnitude (M_c) calculated by $M_c = 5.2 + (\Delta - \Delta_{min}) / (180.0 - \Delta_{min}) - D / D_{max}$, where Δ and D are the epicentral distance in degree and focal depth in kilometer, respectively, $\Delta_{min} = 30^\circ$, and $D_{max} = 700$ km (Liu and Gao, 2010). The requested seismograms were windowed 20 s prior to and 300 s following the arrival of the first theoretical compressional wave phase calculated according to the IASP91 Earth Model (Kennett and Engdahl, 1991). A four-pole, two-pass band-pass Bessel filter with corner frequencies of 0.08 and 0.8 Hz was applied to the original seismograms to enhance the signal-to-noise ratio, and seismograms with a first-arrival signal-to-noise ratio greater than or equal to 4.0 on the vertical component were retained. The remaining seismograms were then converted into radial RFs utilizing the procedure of water level deconvolution of Ammon (1991), with a water level value of 0.03. The resulting 37,089 high-quality RFs were used in the study. RFs from stations that are less than 1.0 km from each other were grouped together, and the combined station was given the name of the station with the most recorded RFs in the group. After station combination, the number of stations reduced from 140 to 115.

2.2. Methods

Some regions of the study area are covered by sediments, pyroclastics, and lava flows up to several kilometers in thickness (Behle et al., 1975; Berckheimer et al., 1975; Lemma et al., 2010; Makris and Ginzburg, 1987). This low velocity layer can cause strong reverberations that may mask the P-to-S converted phases (PmS and multiples) on the RFs (Fig. 3), leading to erroneous H and Vp/Vs measurements (Langston, 2011; Yu et al., 2015; Zelt and Ellis, 1999). Here we apply a resonance-removal filter in the frequency domain (Yu et al., 2015) to remove or significantly reduce the reverberations. For a given RF, the amplitude and the two-way travel time of the reverberation series are determined as the amplitude of the first trough (r_0) and the time delay of the first through (Δt), respectively. The reverberation-removed P-to-S converted phases, $F(i\omega)$, can be obtained in the frequency domain using $F(i\omega) = H(i\omega) / (1 + r_0 \exp(-i\omega\Delta t))$, where ω is angular frequency, $H(i\omega)$ is the spectrum of the RF that contains both the P-to-S converted phases and the reverberations (Yu et al., 2015). The conventional H-Vp/Vs stacking technique (Zhu and Kanamori, 2000) was then employed to determine the optimal H-Vp/Vs pair which corresponds to the maximum stacking amplitude on the H-Vp/Vs plot. The spatially varying searching ranges for H and Vp/Vs are determined with constraints from previous measurements. For all the 30 stations in the WEP and EEP, the searching range for H is 25–45 km with a step of 0.1 km, and that for Vp/Vs is 1.65–2.15 with an interval of 0.01. In the AD and MER, the searching range for H is 15–35 km, and that for Vp/Vs is 1.75–2.35. The only exception is Station AD16 in the AD, where the searching range for Vp/Vs is changed to 1.85–2.45 to make the measurement at this station to be consistent with those from neighboring stations. For a given station, a bootstrap resampling approach (Efron and Tibshirani, 1986) with 10 iterations was employed to obtain the mean and standard deviation of the H and Vp/Vs measurements. For each iteration, $1 - 1/e = 63\%$ RFs are randomly chosen from the original set of RFs recorded by the station. Approximately 60% of the selected RFs are used twice, so that the total number of RFs in the new data set is the same as that in the original one (Liu et al., 2003). Reliable H and Vp/Vs measurements cannot be made at stations that recorded only a limited number (less than 5) of high-quality RFs. Additionally, at some of the stations, the maximum stacking amplitude cannot be unambiguously determined. As a result, among

the 115 stations that recorded one or more RFs, 69 (or 60%) led to reliable H and Vp/Vs measurements. Among those 69 stations, the original RFs from 18 (or 26%) were pre-processed with the reverberation removal filter. Fig. 3 shows examples of the RFs and corresponding H-Vp/Vs plots before and after the removal of the reverberations.

In addition to H and Vp/Vs, the maximum stacking amplitude corresponding to the optimal H-Vp/Vs pair is also measured for each of the stations. The maximum stacking amplitude, R, is a measure of the strength of the PmS and its multiples relative to the amplitude of the direct P wave on the radial components. Several factors may affect the variation of R, including the sharpness of the Moho, the contrast of seismic velocities between the crust and mantle, and the lateral variation in Moho depth (e.g., Bashir et al., 2011; Liu and Gao, 2010; Nair et al., 2006). The sharpness of the Moho is the thickness of the transition layer from the crust to the mantle, and the R will be reduced with the thickening of this layer (e.g., Poppeliers and Datta, 2010). The velocity contrast will influence R value by affecting the acoustic impedance values in the crust and mantle. Variation in Moho depth causes scattering of the PmS phases and consequently reduces their R values (Liu and Gao, 2010).

The selection of a reference average crustal P wave velocity (Vp) is essential for producing reliable H and Vp/Vs measurements using the technique of H-Vp/Vs stacking. Using 27 stations within or adjacent to the MER, the RF study by Dugda et al. (2005) set 6.5 km/s as the reference velocity. Hammond et al. (2011) utilized Vp values ranging from 6.15 to 6.25 km/s for stations in the Afar triple-junction area and the northern portion of the MER. Reed et al. (2014) used a melting function (modified from Watanabe, 1993) to calculate the reference Vp beneath different stations in the AD, which ranges from 4.65 to 5.90 km/s. Stuart et al. (2006) also utilized varying Vp values ranging from 6.1 to 6.5 km/s for stations located in the MER and EP. In this study, we used a constant reference P wave velocity of 6.2 km/s for all the seismic stations, which is consistent with the average crustal Vp estimated from the active-source seismic experiment conducted across the MER and on the EP (Mackenzie et al., 2005; Maguire et al., 2006). According to the synthetic test of Nair et al. (2006), if the used crustal mean Vp is 5% higher than the real value, the H will be overestimated by about 2.5 km, and the Vp/Vs will be underestimated by 0.01. The magnitude of the bias in the resulting H and Vp/Vs is proportional to the magnitude of the bias of the applied Vp. Therefore, the H and Vp/Vs values for a given station obtained by using a constant crustal Vp of 6.2 km/s can be converted into more accurate values when more accurately measured crustal Vp becomes available in the vicinity of the station.

3. Results

Reliable measurements for all the stations can be found in Table S1, and the RFs and H-Vp/Vs plots similar to Fig. 3 for each of the stations are shown in Figs. S1-S69. For the entire study area, the resulting H measurements range from 16.2 km beneath Station HITE in the western part of the AD to 43.0 km beneath Station MECE in the EEP, with an average value of 30.5 ± 7.1 km (Fig. 4). The resulting Vp/Vs measurements range from 1.70 at Station ADYE in the northernmost part of the WEP to 2.35 at Station AD16 in the central part of the AD, with an average value of 1.99 ± 0.16 (Fig. 5). The averaged R value for the entire study area is 0.147 ± 0.054 , with some larger values found along the axes of MER (0.209 ± 0.024 from 5 stations) and RSR (0.229 ± 0.036 from 4 stations) and in the northern part of the WEP (0.173 ± 0.036), and smaller values on the southern part of the WEP (0.126 ± 0.052), and the AD with the exception of the axis of RSR (0.114 ± 0.049) (Fig. 6).

3.1. Western Ethiopian Plateau

For the 24 seismic stations in the WEP, the thickest crust is revealed at Station KORE (42.8 km) located near the northern part of the boundary between the WEP and MER, while this region's thinnest crust

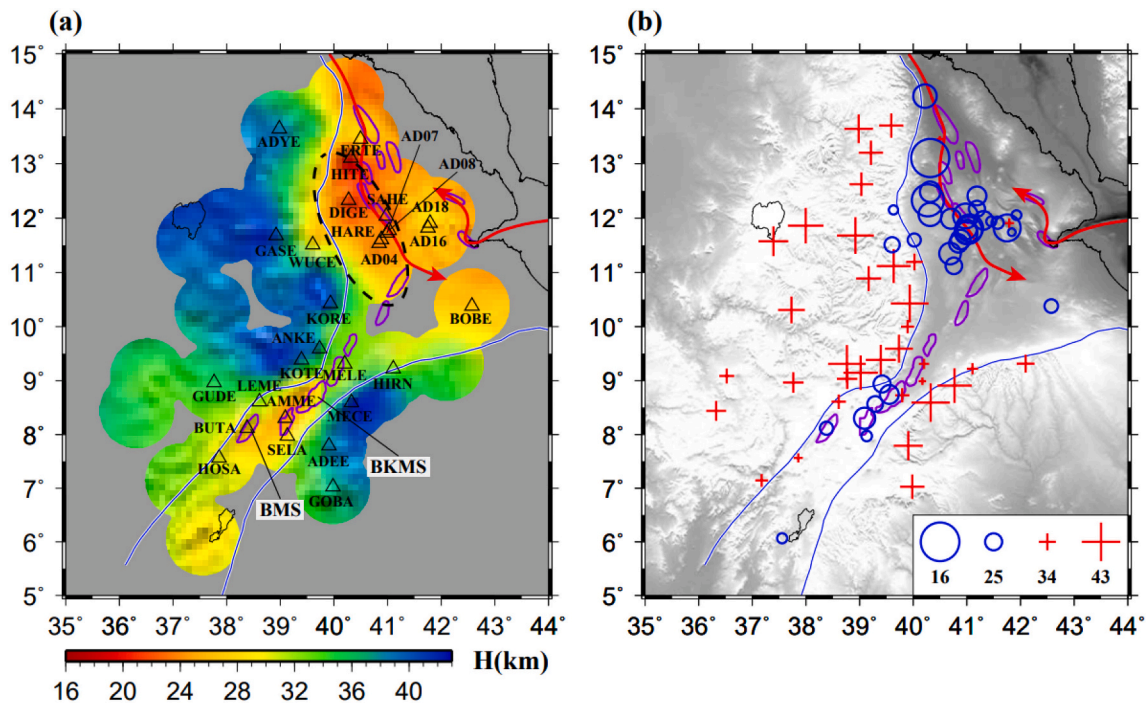


Fig. 4. Resulting H measurements from this study. (a) The results are spatially smoothed and plotted using a continuous colour scale. Open triangles represent stations mentioned in the main text. The black dashed ellipse represents the transition zone between the previous and present axes of the RSR. Magmatic segments within the AD and MER are indicated with purple irregular shapes. BKMS: Boset-Kone magmatic segment; BMS: Butajira magmatic segment. (b) Same as (a) but shows H measurements for all the individual stations. (For interpretation of the references to colour in this figure legend, the reader is referred to the web version of this article.)

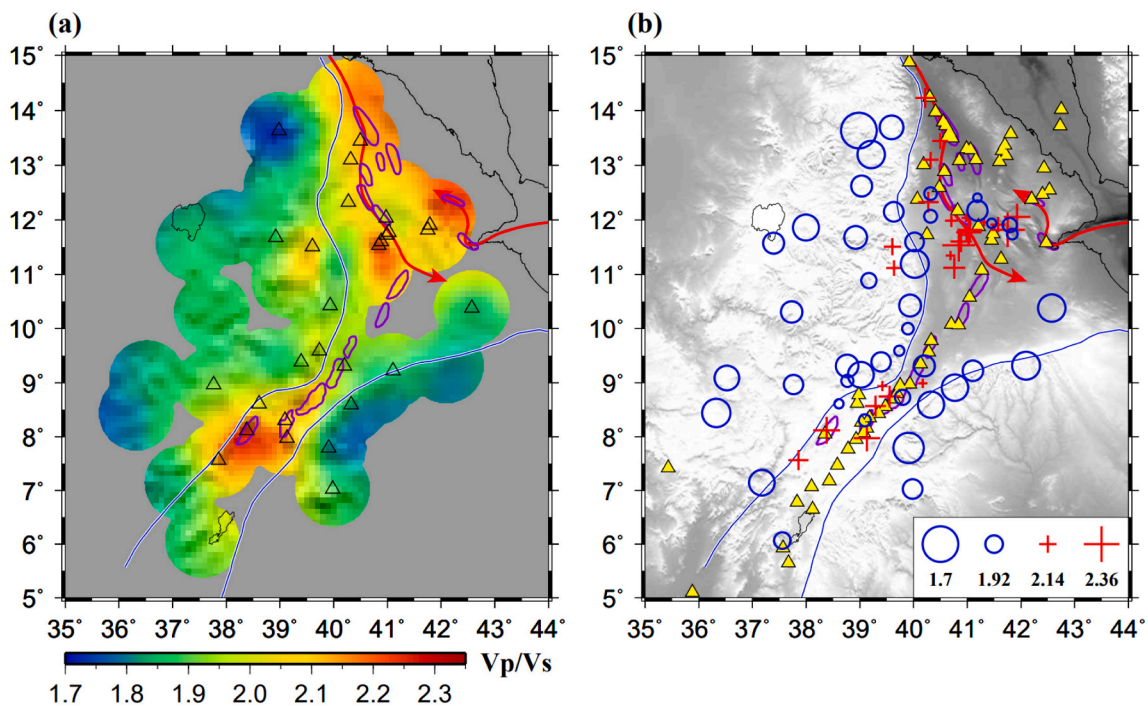


Fig. 5. Resulting Vp/Vs measurements. (a) The results are plotted using a continuous colour scale. Triangles are stations mentioned in the main text when the Vp/Vs results are discussed. The station names can be found in Fig. 4. (b) The results are plotted as pluses and circles. The yellow triangles are active volcanoes. (For interpretation of the references to colour in this figure legend, the reader is referred to the web version of this article.)

of 25.7 km is found beneath Station WUCE near the southern boundary of the WEP and AD (Fig. 4). The mean H value is 36.9 km with a standard deviation of 4.4 km. The resulting Vp/Vs values range from 1.70 at

Station ADYE to 2.14 at Station WUCE with an average value of 1.89 ± 0.10 (Fig. 5). In general, the H values show a decrease while the Vp/Vs measurements show an apparent increase toward the AD and MER. The

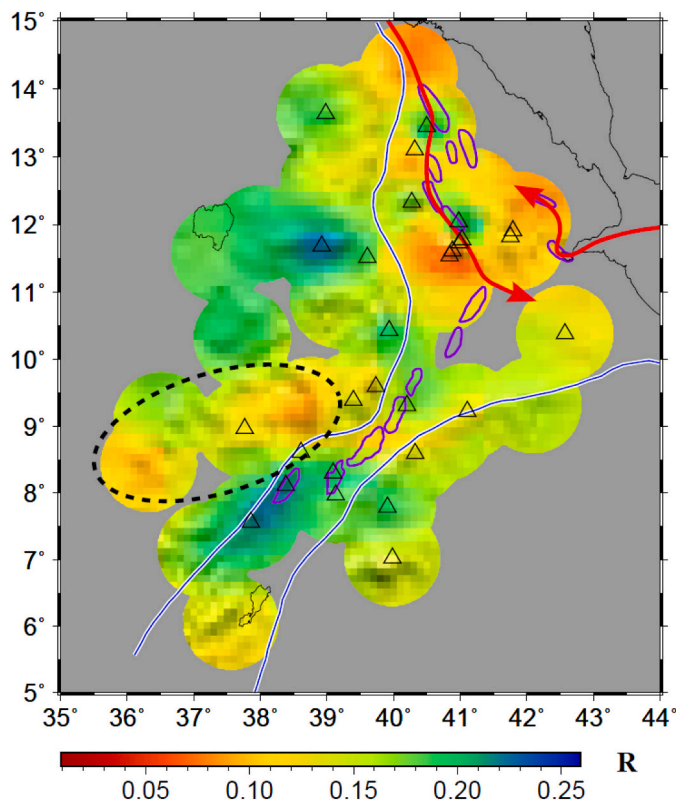


Fig. 6. Resulting R measurements. The black dashed ellipse outlines the low R zone within the southern WEP. Triangles are stations mentioned in the main text when the R measurements are discussed. The station names can be found in Fig. 4.

mean R value in the WEP is 0.156 ± 0.048 . A low R zone with the mean value of 0.098 ± 0.044 is observed in the southern part, and the observed R values generally increase northward reaching a maximum value of 0.245 at Station GASE (Fig. 6).

3.2. Eastern Ethiopian Plateau

The H measured at the 6 stations in the EEP ranges from 31.7 km at Station HIRN located along the northern part of the boundary between the MER and EEP to 43.0 km at Station MECE with an average value of 37.8 ± 4.3 km, which is the largest average value among the four sub-regions. The resulting Vp/Vs measurements range from 1.76 at Station ADEE to 1.89 at Station GOBA near the southern part of the rift-plateau boundary. Both the average Vp/Vs value (1.83) and the corresponding standard deviation (0.05) are the smallest among the four sub-regions. The transition from the thicker crust and lower Vp/Vs in the EEP to the thinner crust and higher Vp/Vs in the adjacent MER takes place over a much shorter distance than that between the WEP and the MER (Figs. 4 and 5). The mean R value in this area is 0.157 ± 0.023 , which is comparable with that in the WEP (Fig. 6).

3.3. Afar depression

The AD has the lowest average H value of 24.2 ± 3.4 km. The minimum value of 16.2 km observed at Station HITE is also the minimum value for the entire study area. The maximum value of 31.0 km is observed at Station AD18 in the central portion of the AD, between the RSR and GAR. Correspondingly, this region has the largest average Vp/Vs value of 2.09 ± 0.13 among the 4 regions in the study area. For most of the 27 stations within the AD, the resulting Vp/Vs measurements are larger than 2.00. The maximum value, which is also the maximum value

for the entire study area, is 2.35 observed at Station AD16, while the minimum Vp/Vs of 1.80 is found at Station BOBE in the southeast corner of the AD. Comparing with the WEP and EEP, the mean R value of 0.131 ± 0.063 is slightly smaller. The RSR has a normal mean R value of 0.148 ± 0.086 with the largest R values concentrated along the axis (e.g., Station AD08: 0.191; Station DIGE: 0.278; Station ERTE: 0.229; Station SAHE: 0.218), and gradually decrease outward (Fig. 6).

3.4. Main Ethiopian Rift

For the 12 stations in the MER, Station AMME in the central part of the MER has the thinnest crust of 23.2 km. Station LEME, located near the boundary between the WEP and the MER, has the thickest crust of 33.0 km. The average H value for this region is 28.2 ± 3.4 km. The smaller standard deviation for H comparing with those in the WEP and EEP reflects a small lateral variations of H. The resulting Vp/Vs measurements are between 1.88 at Station MELE and 2.26 at Station BUTA with an average value of 2.08 ± 0.13 . The mean R value of 0.163 ± 0.048 is the largest comparing with the other three sub-regions. Large R values are mainly observed near the magmatic segments along the rift axis (e.g., Station MELE: 0.199; Station AMME: 0.217; Station SELA: 0.172; Station BUTA: 0.221; Station HOSA: 0.234), and there is a clear boundary in the spatial distribution of the R values between the southern MER and the WEP and EEP (Fig. 6).

4. Discussion

4.1. Comparison with previous studies

Forty broadband seismic stations located mainly in the MER, EEP, and southern portion of the WEP, from the EAGLE and EBSE projects, were utilized by Stuart et al. (2006) to calculate H and Vp/Vs values. Twenty-two out of the 40 stations were used by our study. Fig. 7a and b show comparison of the results at the 22 common stations. Reverberation removal filters were applied to 10 of the common stations (red circles in Fig. 7a and b). The mean H at the common stations is 36.3 ± 4.4 km in Stuart et al. (2006), and 33.5 ± 6.1 km in our study. The mean Vp/Vs is 1.91 ± 0.12 in Stuart et al. (2006), and 1.97 ± 0.14 in our study. Two possible factors may be responsible for the slight discrepancies in the results. First, the reference velocity used to calculate the H by Stuart et al. (2006), either 6.25 km/s or 6.50 km/s for the 10 common stations that we processed using the reverberation removal filter, is higher than the value of 6.20 km/s used in the present study. This ~1%–5% difference in the mean crustal Vp results in an over-estimated H by 0.5–2.5 km, and an under-estimated Vp/Vs by 0.002–0.01 (Nair et al., 2006). Additionally, for stations atop a low-velocity sedimentary layer, the amplitude of the first P-to-S phase from the bottom of the sedimentary layer can mask the direct P wave, leading to a delayed first peak on the RFs (Yeck et al., 2013), which in turn results in greater H.

For the AD and the northern portion of the WEP, Hammond et al. (2011) conducted H and Vp/Vs measurements at 48 stations belonging to the AFAR project. We obtained reliable H and Vp/Vs measurements at 22 seismic stations, among which the reverberation-removal filter was applied to five stations. The mean H at the common stations in Hammond et al. (2011) is 29.9 ± 7.5 km, and in our study it is 29.6 ± 7.4 km. Generally our resulting Vp/Vs measurements are more consistent with those of Hammond et al. (2011) than results in Stuart et al. (2006), and the largest discrepancy is observed at Station HARE (Fig. 7d). Our resulting Vp/Vs measurement for Station HARE is 2.19, while it is 1.99 in Hammond et al. (2011). For the three stations (AD04, AD07, and AD08) that are within 25 km from Station HARE, our measured Vp/Vs values are 2.33, 2.07, and 2.24, respectively. Our resulting Vp/Vs measurement at Station HARE (2.19) is more consistent with these values. Additionally, the reverberation-removal filter has been applied to HARE (Fig. S49). When the original RFs are used, the resulting Vp/Vs value is 1.82, which is inconsistent with nearby stations. Therefore, the

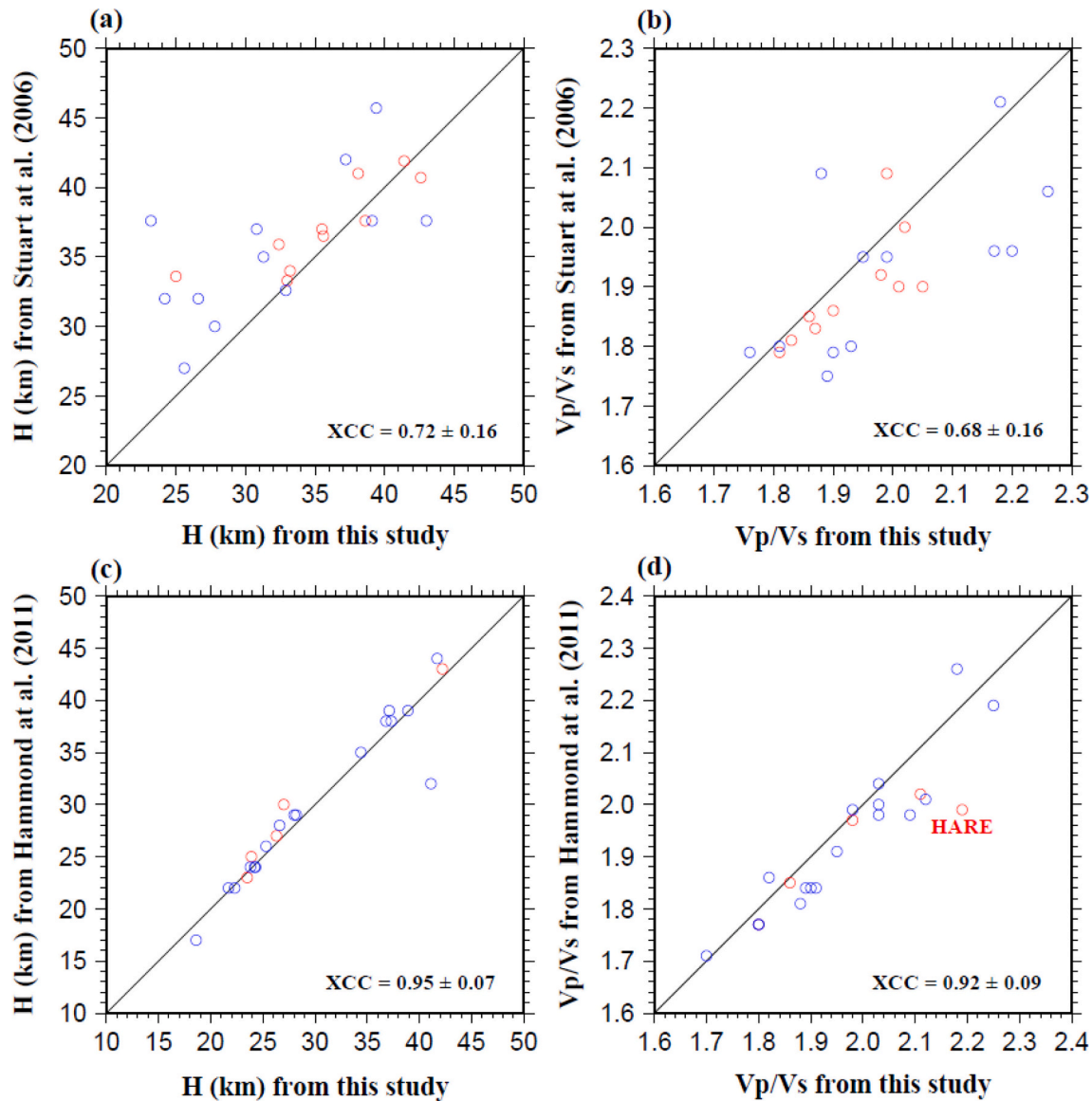


Fig. 7. Comparisons of H and Vp/Vs measurements obtained in this study and those in previous RF studies. (a) Comparison of H measurements between this study and that of [Stuart et al. \(2006\)](#). Red symbols represent stations that were processed with the reverberation removal filter, and blue symbols represent ones that were not processed with the filter. (b) Same as (a) but for comparison of Vp/Vs measurements. (c) and (d) Same as (a) and (b), respectively, but for measurements in [Hammond et al. \(2011\)](#). XCC stands for cross-correlation coefficient. (For interpretation of the references to colour in this figure legend, the reader is referred to the web version of this article.)

discrepancy can be possibly attributed to the strong sedimentary reverberation at the station.

Our mean R value for the entire study area (0.147 ± 0.054) is comparable with that measured in the stable Archean cratons in southern Africa by [Nair et al. \(2006\)](#). According to [Nair et al. \(2006\)](#), the mean R for the Kaapvaal and Zimbabwe cratons and the Limpopo Belt in southern Africa is 0.141 ± 0.058 . The highest mean R of 0.176 ± 0.062 is observed in the Kaapvaal Craton with the exception of Bushveld Complex (0.112 ± 0.035), which is believed to be underlain by a 12-km-thick mantle-derived mafic layer beneath the Moho. The decreased velocity contrast across the Moho is mostly responsible for the reduction in R ([Nair et al., 2006](#)). In the Zimbabwe Craton, a significant difference in R values is detected between the NE and SW portions of the craton, with mean values of 0.135 ± 0.027 in the former and 0.070 ± 0.013 in the latter area. The difference may be caused by the magmatic intrusion from the mafic Okavango dyke swarm and the associated lithospheric refertilization in the southwestern part of the craton ([Nair et al., 2006](#); [Wang et al., 2019](#)). Because the density of the intruded mantle materials

is most likely higher than that of the lowermost crust, the density contrast across the Moho reduces, leading to smaller R values. On the other hand, refertilization of the uppermost mantle could decrease the seismic velocities by reintroducing the previously depleted elements (e. g., Fe and Mg), which could also reduce the velocity contrast between the uppermost mantle and the overlying crust, resulting in smaller R values.

The Colorado Plateau is characterized by a mean R value of 0.105 ± 0.007 which is lower than that in the Basin and Range Province (0.181 ± 0.014) ([Bashir et al., 2011](#)). The R measurements obtained on the Colorado Plateau are smaller than those obtained on both the WEP (0.156 ± 0.048) and the EEP (0.157 ± 0.023). A 12-km thick, mechanically strong, mafic lowermost crustal layer with high Vp/Vs values (~ 2.05) estimated by [Bashir et al. \(2011\)](#) is proposed to be responsible for the observed low R values in the Colorado Plateau. At Station TAM on the Hoggar Swell in NW Africa, the R value in the volcanic Tefedest terrane is 0.156 ± 0.003 , which is comparable to typical cratonic areas, while that in the non-volcanic Laouni terrane is 0.037 ± 0.003 ([Liu and Gao,](#)

2010). The R value in the Laouni terrane is slightly smaller than our measured R values of ~ 0.070 in the southern WEP and AD with the exception of those along the axis of the RSR (Fig. 6). Liu and Gao (2010) attributed the low R value to an underplated mafic layer beneath the Moho. These R observations obtained in a diverse set of tectonic environments provide insights for interpreting the anomalously small R measurements in the study area.

4.2. Widespread magmatic intrusion and partial melting

For the study area, the V_p/V_s values range from 1.70 to 2.35 with a mean value of 1.98 ± 0.15 , which is significantly (about 11%) higher than the mean value of 1.78 for continental crust (Christensen, 1996). Several factors may be responsible for the higher-than-normal V_p/V_s values (Fig. 8), including:

1). Contribution from a layer of continental flood basalts that is pervasively present in this region (e.g., Pik et al., 1998; Rooney, 2017). Assuming a V_p/V_s of 1.84 for basalt and a normal crustal V_p/V_s of 1.78

(Christensen, 1996), we estimated that a 2–5 km thick layer of basalts would lead to an increase of $\sim 0.2\% - 0.5\%$ in V_p/V_s for a 35 km crust.

2). Intrusion of basaltic magma through diking. In the WEP and EEP, Jestin and Huchon (1992) proposed that fissure-fed continental flood basalts erupted before the main tectonic phases of rifting. In the AD, magma injections into the upper crust beneath magmatic segments were observed by previous studies (e.g., Ayele et al., 2007; Grandin et al., 2010). The Miocene and Plio-Quaternary volcanism in the AD and MER located along the rift axis is more likely related to central vent-type eruptions due to the larger amount of stretching and extension of the crust (Pik et al., 1998). This is consistent with our H and V_p/V_s measurements, which show thinner crust and higher V_p/V_s within the AD and MER (Figs. 4 and 5).

3). Wide-spread crustal partial melting. For most of the study area, the observed V_p/V_s is higher than the value of 1.84 for solid basalt (Christensen, 1996), suggesting that intrusion and extrusion of basaltic magma alone cannot account for the large V_p/V_s measurements. Theoretical calculations demonstrate that crustal V_p/V_s is a continuous

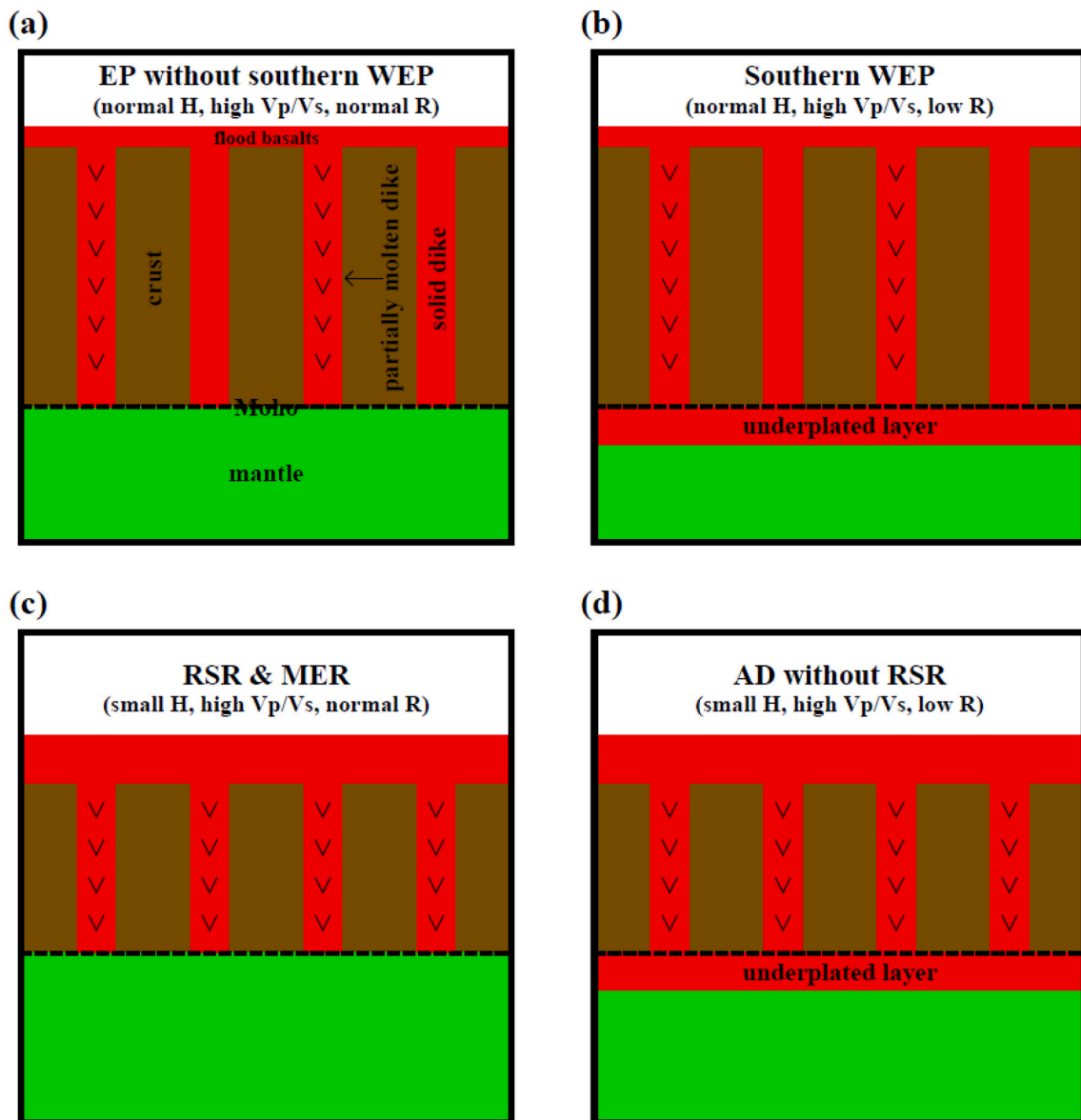


Fig. 8. Schematic diagrams showing the structure of the crust and uppermost mantle. (a) Beneath the EP with the exception of southern part of the WEP, (b) beneath the WEP, (c) beneath the RSR and MER, and (d) beneath the AD with the exception of the RSR. Dikes with arrows represent partially molten ones, while those without arrows represent solid ones.

function of melt fraction (Watanabe, 1993). Such a dependence is exponential for crustal silicates, e.g., the V_p/V_s is about 1.82 for 0% melt and 1.90 for 5% melt, and increases to 2.05 at 10% melt (Reed et al., 2014; Watanabe, 1993). While it is difficult to isolate the contributions of partial melt from the other factors on the increasing in V_p/V_s , the large V_p/V_s values observed beneath the AD, MER, and most portions of the WEP suggest the presence of wide-spread partial melting in the crust. The highest melt fraction is inferred in the AD and MER, where numerous active volcanoes are present (Fig. 5b). In the MER, the Boset-Kone and Butajira magmatic segments are characterized by highest V_p/V_s and thinnest crust, respectively (Figs. 4 and 5). Eruption of the Kone volcano in the Boset-Kone magmatic segment occurred as recently as 1810 CE (Harris, 1844). Controlled-source seismic tomography studies (e.g., Keranen et al., 2004; Mackenzie et al., 2005) indicate that P wave velocities of the upper crust (10 km depth) beneath the Boset-Kone and Butajira magmatic segments are 5% - 10% higher than those outside the magmatic segment, suggesting the presence of mafic intrusions in the upper crust associated with the magmatic segments, an observation that is also supported by a magnetotelluric study (Whaler and Hautot, 2006). These observations are consistent with the existence of a higher fraction of partial melt beneath the two magmatic segments than the other areas in the MER.

4.3. Migration of the extension center of the Red Sea Rift

The extension rates between the Nubian and Arabian plates, the Arabian and Somalian plates, and the Nubian and Somalian plates are ~ 16 mm/yr, ~ 18 mm/yr, and 3–6 mm/yr, respectively (Bendick et al., 2006; Bilham et al., 1999; Vigny et al., 2006). Due to the differences in the extension rates, the Afar triple junction has migrated northeastward by ~ 160 km during the past 10 Myr (Kalb, 1995; McKenzie and Morgan, 1969). The previous N-S orientated RSR has rotated into a NW-SE orientation due to the migration of the triple junction, forming a transition zone to the southwest of the present rift axis (Fig. 4a). The RF study by Hammond et al. (2011) supported the hypothesis of northeastward migration of the RSR. Due to the existence of thicker crust (~ 33.0 km) and lower V_p/V_s (~ 1.88) at the RSR transition zone, which suggests the inadequacy of partial melt, Hammond et al. (2011) proposed that the RSR rift axis may have migrated from the previous to its current positions in a discrete (“jumpy”) fashion.

Our results show pervasively thinned crust of ~ 24.0 km (Fig. 4) and high V_p/V_s values of ~ 2.20 (Fig. 5) in the transition zone of the rift migration. The resulting H and V_p/V_s measurements indicate the presence of gradual variation of partial melt beneath the transition zone, which in turn suggests a gradual-migration rather than a jumpy-migration model. A gradual variation in melt fraction from the southwest of the rift axis to the center of the axis observed by Reed et al. (2014) also indicates the pervasive existence of partial melt.

4.4. Implications of the low stacking amplitude

A couple of tectonically significant implications can be drawn from the spatial distribution of the R measurements (Fig. 6). First, low R values observed in the southern WEP (0.098 ± 0.044) and AD with the exception of the RSR (0.114 ± 0.049) may indicate a reduced velocity contrast across the Moho beneath the area. While significant Moho tilting and undulation can also reduce R (e.g., Liu and Gao, 2010), our resulting H values suggest that the Moho is probably a fairly flat interface in both regions (Fig. 4), suggesting the low R values are not likely to be caused by lateral variation in Moho depth. Similarly, synthetic studies indicate that the PmS phase would be broadened if the reduced R is associated with a reduction in Moho sharpness (Poppeliers and Datta, 2010). However, such a broadening is not systematically observed at stations with low R values. Thus, the low R values are unlikely caused by a reduction in Moho sharpness. Therefore, reduced velocity contrast across the Moho is most likely responsible for the low R. Comparing with

tectonically stable cratonic areas such as the Kaapvaal and Zimbabwe cratons (Nair et al., 2006), the relatively low R values can be explained by the existence of a magmatic underplated layer beneath the Moho (Fig. 8b and d). Here we define underplating as a process that produces a layer of mantle-derived magma that is trapped below the Moho and spread horizontally (e.g., Cox, 1993). The existence of an underplated layer, which has a P wave velocity that is higher than that for the lowermost crust but lower than that for the uppermost mantle (Keller et al., 1994; Liu and Gao, 2010; Voss and Jokat, 2007), will reduce the velocity contrast through the Moho, and subsequently lower the R values.

Second, among the entire AD, normal stacking amplitude values are observed beneath the volcanic segments that are mainly along the RSR, indicating possible absence of underplating. Unlike the rest of the AD, the mantle-derived magma beneath the RSR directly reaches the surface rather than being trapped beneath the Moho, forming a sharp Moho and leading to normal R values. The same process may also be responsible for the normal or higher-than-normal R values observed in the volcanic segments along the MER (Figs. 6 and 8c). This difference in the emplacement depth of the magma between the rifted areas and the rest (Fig. 8) is consistent with the existence of a thicker basaltic layer atop the crust in the RSR and MER (e.g., Mackenzie et al., 2005; Maguire et al., 2006; Makris and Ginzburg, 1987).

5. Conclusions

Using all the available broadband seismic data recorded in the Afar Depression, the Main Ethiopian Rift, and the Ethiopian Plateau, we delineate systematic spatial variations in crustal thickness, V_p/V_s , and amplitude of P-to-S converted phases from the Moho. The anomalously high V_p/V_s values across most of the study area is associated with the presence of continental flood basalts atop the crust, magmatic diking, and partial melt in the crust. High V_p/V_s and significant crustal thinning beneath the transition zone between the old and new axes of the Red Sea Rift are in agreement with a gradual migration model of the rift axis, and low stacking amplitudes observed beneath the southern part of the western Ethiopian Plateau and Afar Depression with the exception of the Red Sea Rift can be explained by the existence of an underplated magmatic layer.

Declaration of Competing Interest

The authors declare that they have no known competing financial interests or personal relationships that could have appeared to influence the work reported in this paper.

Acknowledgments

All the data used in this study are publicly available from the IRIS DMC (<https://ds.iris.edu/ds/nodes/dmc>, with the following doi: <https://doi.org/10.1029/2002EO000296>; <https://doi.org/10.1029/2003EO350002>; <https://doi.org/10.1002/2013JB010719>. Last accessed: December 2018). This study was partially supported by the U. S. National Science Foundation grants 1009946 and 1460516 to S.G. and K.H., 1919789 to S.G., and by the American Chemical Society grant PRF-60281-ND8 to S.G.

Appendix A. Supplementary data

Supplementary data to this article can be found online at <https://doi.org/10.1016/j.tecto.2021.228857>.

References

- Ammon, C.J., 1991. The isolation of receiver effects from teleseismic P waveforms. *Bull. Seismol. Soc. Am.* 81 (6), 2,504–2,510.

- Audin, L., Manighetti, I., Tapponnier, P., Metivier, F., Jacques, E., Huchon, P., 2001. Fault propagation and climatic control of sedimentation on the Ghoubbet Rift Floor: Insights from the Tadjouraden cruise in the western Gulf of Aden. *Geophys. J. Int.* 144 (2), 391–413. <https://doi.org/10.1046/j.0956-540x.2000.01322.x>.
- Ayele, A., Stuart, G., Kendall, J.-M., 2004. Insights into rifting from shear wave splitting and receiver functions: an example from Ethiopia. *Geophys. J. Int.* 157 (1), 354–362. <https://doi.org/10.1111/j.1365-246X.2004.02206.x>.
- Ayele, A., Jacques, E., Kassim, M., Kidane, T., Omar, A., Tait, S., Nercessian, A., de Chabaliere, J.-B., King, G., 2007. The volcano-seismic crisis in Afar, Ethiopia, starting September 2005. *Earth Planet. Sci. Lett.* 255 (1–2), 177–187. <https://doi.org/10.1016/j.epsl.2006.12.014>.
- Barberi, F., Varet, J., 1977. Volcanism of Afar: Small-scale plate tectonics implications. *Geol. Soc. Am. Bull.* 88 (9), 1,251–1,266. [https://doi.org/10.1130/0016-7606\(1977\)88<1251:VOASPT>2.0.CO;2](https://doi.org/10.1130/0016-7606(1977)88<1251:VOASPT>2.0.CO;2).
- Bashir, L., Gao, S.S., Liu, K.H., Mickus, K., 2011. Crustal structure and evolution beneath the Colorado Plateau and the southern Basin and Range Province: results from receiver function and gravity studies. *Geochem. Geophys. Geosyst.* 12 (6), Q06008 <https://doi.org/10.1029/2011GC003563>.
- Bastow, I.D., Keir, D., 2011. The protracted development of the continent-ocean transition in Afar. *Nat. Geosci.* 4 (4), 248–250. <https://doi.org/10.1038/ngeo1095>.
- Behle, A., Makris, J., Baier, J., Delibasis, N., 1975. Salt thickness near Dallol (Ethiopia) from seismic reflection measurements and gravity data. In: *Afar Depression of Ethiopia: Proceedings of an International Symposium on the Afar Region and Related Rift Problems, Held in Bad Bergzabern, FR Germany, April 1–6, 1974*. Schweizerbart, Stuttgart, Germany, pp. 156–167.
- Bendick, R., McClusky, S., Bilham, R., Asfaw, L., Klemperer, S., 2006. Distributed Nubia-Somalia relative motion and dike intrusion in the Main Ethiopian Rift. *Geophys. J. Int.* 165 (1), 303–310. <https://doi.org/10.1111/j.1365-246X.2006.02904.x>.
- Berckhemer, H., Baier, B., Bartelsen, H., Behle, A., Burckhardt, H., Gebrande, H., Makris, J., Menzel, J., Miller, H., Veas, R., 1975. Deep seismic soundings in the Afar region and on the highlands of Ethiopia. In: *Afar Depression of Ethiopia: Proceedings of an International Symposium on the Afar Region and Related Rift Problems, Held in Bad Bergzabern, FR Germany, April 1–6, 1974*. Schweizerbart, Stuttgart, Germany, pp. 89–107.
- Beyene, A., Abdelsalam, M.G., 2005. Tectonics of the Afar Depression: A review and synthesis. *J. Afr. Earth Sci.* 41 (1–2), 41–59. <https://doi.org/10.1016/j.jafrearsci.2005.03.003>.
- Bilham, R., Bendick, R., Larson, K., Mohr, P., Braun, J., Tesfaye, S., Asfaw, L., 1999. Secular and tidal strain across the Main Ethiopian Rift. *Geophys. Res. Lett.* 26 (18), 2,789–2,792. <https://doi.org/10.1029/1998GL005315>.
- Bridges, D.L., Mickus, K., Gao, S.S., Abdelsalam, M.G., Alemu, A., 2012. Magnetic stripes of a transitional continental rift in Afar. *Geology* 40 (3), 203–206. <https://doi.org/10.1130/G32697.1>.
- Chambers, E.L., Harmon, N., Keir, D., Rychert, C.A., 2019. Using Ambient Noise to image the Northern East African Rift. *Geochim. Geophys. Geosyst.* 20 (4), 2,091–2,109. <https://doi.org/10.1029/2018GC008129>.
- Christensen, N.I., 1996. Poisson's ratio and crustal seismology. *J. Geophys. Res. Solid Earth* 101 (B2), 3,139–3,156. <https://doi.org/10.1029/95JB03446>.
- Chu, D., Gordon, R.G., 1998. Current plate motions across the Red Sea. *Geophys. J. Int.* 135 (2), 313–328. <https://doi.org/10.1046/j.1365-246X.1998.00658.x>.
- Courtillot, V., Achange, J., Landre, F., Bonhommet, N., Montigny, R., Feraud, G., 1984. Episodic spreading and rift propagation: New paleomagnetic and geochronologic data from the Afar Nascent passive margin. *J. Geophys. Res. Solid Earth* 89 (B5), 3,315–3,333. <https://doi.org/10.1029/JB089B05p03315>.
- Courtillot, V., Armijo, R., Tapponnier, P., 1987. Kinematics of the Sinai triple junction and a two-phase model of Arabia-Africa rifting. *Geol. Soc. Spec. Publ.* 28 (1), 559–573. <https://doi.org/10.1144/GSL.SP.1987.028.01.37>.
- Cox, K.G., 1993. Continental magmatic underplating. *Philos. Trans. R. Soc. A* 342 (1663), 155–166. <https://doi.org/10.1098/rsta.1993.0011>.
- d'Acremont, E., Leroy, S., Beslier, M.-O., Bellahsen, N., Fournier, M., Robin, C., Maia, M., Gente, P., 2005. Structure and evolution of the eastern Gulf of Aden conjugate margins from seismic reflection data. *Geophys. J. Int.* 160 (3), 869–890. <https://doi.org/10.1111/j.1365-246X.2005.02524.x>.
- Davidson, A., Rex, D.C., 1980. Age of volcanism and rifting in southwestern Ethiopia. *Nature* 283 (5748), 657–658. <https://doi.org/10.1038/283657a0>.
- Dugda, M.T., Nyblade, A.A., Julia, J., Langston, C.A., Ammon, C.J., Simiyu, S., 2005. Crustal structure in Ethiopia and Kenya from receiver function analysis: Implications for rift development in eastern Africa. *J. Geophys. Res. Solid Earth* 110 (1), 1–15. <https://doi.org/10.1029/2004JB003065>. B01303.
- Dugda, M.T., Nyblade, A.A., Julia, J., 2007. Thin lithosphere beneath the Ethiopian Plateau revealed by a joint inversion of Rayleigh wave group velocities and receiver functions. *J. Geophys. Res. Solid Earth* 112 (8), B08305. <https://doi.org/10.1029/2006JB004918>.
- Ebinger, C.J., Casey, M., 2001. Continental breakup in magmatic provinces: An Ethiopian example. *Geology* 29 (6), 527–530. [https://doi.org/10.1130/0091-7613\(2001\)029<0527:CBIMPA>2.0.CO;2](https://doi.org/10.1130/0091-7613(2001)029<0527:CBIMPA>2.0.CO;2).
- Ebinger, C.J., Yemane, T., WoldeGabrial, G., Aronson, J.L., Walter, R.C., 1993. Late Eocene-recent volcanism and faulting in the southern main Ethiopian rift. *J. Geol. Soc.* 150 (1), 99–108. <https://doi.org/10.1144/gsjgs.150.1.0099>.
- Efron, B., Tibshirani, R., 1986. Bootstrap methods for standard errors, confidence intervals, and other measures of statistical accuracy. *Stat. Sci.* 1 (1), 54–75. <https://doi.org/10.1214/ss/1177013815>.
- Grandin, R., Socquet, A., Doin, M.-P., Jacques, E., de Chabaliere, J.-B., King, G.C.P., 2010. Transient rift opening in response to multiple dike injections in the Manda Hararo rift (Afar, Ethiopia) imaged by time-dependent elastic inversion of interferometric synthetic aperture radar data. *J. Geophys. Res. Solid Earth* 115 (B9). <https://doi.org/10.1029/2009JB006883>.
- Guidarelli, M., Stuart, G., Hammond, J.O.S., Kendall, J.M., Ayele, A., Belachew, M., 2011. Surface wave tomography across Afar, Ethiopia: Crustal structure at a rift triple-junction zone. *Geophys. Res. Lett.* 38 (24), L24313 <https://doi.org/10.1029/2011GL046840>.
- Hammond, J.O.S., Kendall, J.-M., Stuart, G.W., Keir, D., Ebinger, C., Ayele, A., Belachew, M., 2011. The nature of the crust beneath the Afar triple junction: Evidence from receiver functions. *Geochem. Geophys. Geosyst.* 12 (12), Q12004 <https://doi.org/10.1029/2011GC003738>.
- Harris, W.C., 1844. *The Highlands of Ethiopia*, vol. 3. Langman, Brown and Langman, London.
- Hayward, N.J., Ebinger, C.J., 1996. Variations in the along-axis segmentation of the Afar Rift system. *Tectonics* 15 (2), 244–257. <https://doi.org/10.1029/95TC02292>.
- Hofmann, C., Courtillot, V., Feraud, G., Rochette, P., Yirgu, G., Ketefo, E., Pik, R., 1997. Timing of the Ethiopian flood basalt event and implications for plume birth and global change. *Nature* 389 (6653), 838–841. <https://doi.org/10.1038/39853>.
- Jestin, F., Huchon, P., 1992. Cinématique et déformation de la jonction triple Mer Rouge, golfe d'Aden, rift éthiopien depuis l'Oligocène. *Bull. Soc. Geol. Fr.* 163 (2), 125–133.
- Kalb, J.E., 1995. Fossil elephantoids, Awash paleolake basins, and the Afar triple junction, Ethiopia. *Palaeogeogr. Palaeoclimatol. Palaeoecol.* 114 (2–4), 357–368. [https://doi.org/10.1016/0031-0182\(94\)00088-P](https://doi.org/10.1016/0031-0182(94)00088-P).
- Keller, G.R., Prodehl, C., Mechie, J., Fuchs, K., Khan, M.A., Maguire, P.K.H., Mooney, W. D., Achauer, U., Davis, P.M., Meyer, R.P., Braille, L.W., Nyambok, I.O., Thompson, G. A., 1994. The East African rift system in the light of KRISP 90. *Tectonophysics* 236 (1–4), 465–483. [https://doi.org/10.1016/0040-1951\(94\)90190-2](https://doi.org/10.1016/0040-1951(94)90190-2).
- Kennett, B.L.N., Engdahl, E.R., 1991. Traveltimes for global earthquake location and phase identification. *Geophys. J. Int.* 105 (2), 429–465. <https://doi.org/10.1111/j.1365-246X.1991.tb06724.x>.
- Keranen, K., Klemperer, S.L., Gloaguen, R., EAGLE Working Group, 2004. Three-dimensional seismic imaging of a proteridic axis in the Main Ethiopian rift. *Geology* 32 (11), 949–952. <https://doi.org/10.1130/G20737.1>.
- Keranen, K.M., Klemperer, S.L., Julia, J., Lawrence, J.F., Nyblade, A.A., 2009. Low lower crustal velocity across Ethiopia: Is the Main Ethiopian Rift a narrow rift in a hot craton? *Geochem. Geophys. Geosyst.* 10 (5) <https://doi.org/10.1029/2008GC002293>.
- Kibret, B.A., Ayele, A., Keir, D., 2019. Crustal thickness estimates beneath four seismic stations in Ethiopia inferred from P-wave receiver function studies. *J. Afr. Earth Sci.* 150, 264–271. <https://doi.org/10.1016/j.jafrearsci.2018.11.005>.
- Kim, S., Nyblade, A.A., Rhie, J., Baag, C.-E., Kang, T.-S., 2012. Crustal S-wave velocity structure of the Main Ethiopian Rift from ambient noise tomography. *Geophys. J. Int.* 191 (2), 865–878. <https://doi.org/10.1111/j.1365-246X.2012.05664.x>.
- Langston, C.A., 2011. Wave-field continuation and decomposition for passive seismic imaging under deep unconsolidated sediments. *Bull. Seismol. Soc. Am.* 101 (5), 2,176–2,190. <https://doi.org/10.1785/0120100299>.
- Lemma, Y., Hailu, A., Desissa, M., Kalberkamp, U., 2010. Integrated Geophysical Surveys to Characterize Tendaho Geothermal Field in North Eastern Ethiopia. *World Geothermal Congress, Indonesian Geothermal Association, Bali, Indonesia*.
- Liu, K.H., Gao, S.S., 2010. Spatial variations of crustal characteristics beneath the Hoggar swell, Algeria, revealed by systematic analyses of receiver functions from a single seismic station. *Geochem. Geophys. Geosyst.* 11 (8), Q08011 <https://doi.org/10.1029/2010GC003091>.
- Liu, K.H., Gao, S.S., Silver, P.G., Zhang, Y., 2003. Mantle layering across central South America. *J. Geophys. Res. Solid Earth* 108 (B11), 2510. <https://doi.org/10.1029/2002JB002208>.
- Mackenzie, G.D., Thybo, H., Maguire, P.K.H., 2005. Crustal velocity structure across the Main Ethiopian Rift: Results from two-dimensional wide-angle seismic modelling. *Geophys. J. Int.* 162 (3), 994–1,006. <https://doi.org/10.1111/j.1365-246X.2005.02710.x>.
- Maguire, P.K.H., Ebinger, C.J., Stuart, G.W., Mackenzie, G.D., Whaler, K.A., Kendall, J.-M., Khan, M.A., Fowler, C.M.R., Klemperer, S.L., Keller, G.R., Harder, S., Furman, T., Mickus, K., Asfaw, L., Ayele, A., Abebe, B., 2003. Geophysical project in Ethiopia studies continental breakup. *EOS Trans. AGU* 84 (35), 337–343. <https://doi.org/10.1029/2003EO350002>.
- Maguire, P.K.H., Keller, G.R., Klemperer, S.L., Mackenzie, G.D., Keranen, K., Harder, S., O'Reilly, B., Thybo, H., Asfaw, L., Khan, M.A., Amha, M., 2006. Crustal structure of the northern Main Ethiopian Rift from the EAGLE controlled-source survey; a snapshot of incipient lithospheric breakup. *Geol. Soc. Spec. Publ.* 259, 269–292. <https://doi.org/10.1144/GSL.SP.2006.259.01.21>.
- Makris, J., Ginzburg, A., 1987. The Afar Depression: Transition between continental rifting and sea-floor spreading. *Tectonophysics* 141 (1–3), 199–214. [https://doi.org/10.1016/0040-1951\(87\)90186-7](https://doi.org/10.1016/0040-1951(87)90186-7).
- Manighetti, I., Tapponnier, P., Courtillot, V., Gruszow, S., Gillot, P.-Y., 1997. Propagation of rifting along the Arabia-Somalia plate boundary: The Gulfs of Aden and Tadjoura. *J. Geophys. Res. Solid Earth* 102 (B2), 2,681–2,710. <https://doi.org/10.1029/96JB01185>.
- Manighetti, I., Tapponnier, P., Gillot, P.-Y., Jacques, E., Courtillot, V., Armijo, R., Ruegg, J.C., King, G., 1998. Propagation of rifting along the Arabia-Somalia plate boundary: Into Afar. *J. Geophys. Res. Solid Earth* 103 (B3), 4,947–4,974. <https://doi.org/10.1029/97JB02758>.
- McKenzie, D.P., Morgan, W.J., 1969. Evolution of triple junctions. *Nature* 224 (5215), 125–133. <https://doi.org/10.1038/224125a0>.
- McKenzie, D.P., Davies, D., Molnar, P., 1970. Plate tectonics of the Red Sea and East Africa. *Nature* 226 (5242), 243–248. <https://doi.org/10.1038/226243a0>.
- Mohr, P.A., Zanettin, B., 1988. *The Ethiopian flood basalt province*. In: *Macdougall, J.D. (Ed.), Continental Flood Basalts*. Kluwer, Dordrecht, pp. 63–110.

- Nair, S.K., Gao, S.S., Liu, K.H., Silver, P.G., 2006. Southern African crustal evolution and composition: Constraints from receiver function studies. *J. Geophys. Res. Solid Earth* 111 (2), B02304. <https://doi.org/10.1029/2005JB003802>.
- Nyblade, A.A., Langston, C.A., 2002. Broadband seismic experiments probe the East African rift. *EOS Trans. AGU* 83 (37), 405, 408–409. <https://doi.org/10.1029/2002EO0000296>.
- Pik, R., Deniel, C., Coulon, C., Yirgu, G., Hofmann, C., Ayalew, D., 1998. The northwestern Ethiopian Plateau flood basalts: Classification and spatial distribution of magma types. *J. Volcanol. Geotherm. Res.* 81 (1–2), 91–111. [https://doi.org/10.1016/S0377-0273\(97\)00073-5](https://doi.org/10.1016/S0377-0273(97)00073-5).
- Poppeliers, C., Datta, T., 2010. The effects of crustal heterogeneity on ray-based teleseismic imaging. *Geophys. J. Int.* 181 (2), 1,041–1,061. <https://doi.org/10.1111/j.1365-246X.2010.04555.x>.
- Reed, C.A., Almadani, S., Gao, S.S., Elsheikh, A.A., Cherie, S., Abdelsalam, M.G., Thurmond, A.K., Liu, K.H., 2014. Receiver function constraints on crustal seismic velocities and partial melting beneath the Red Sea rift and adjacent regions, Afar Depression. *J. Geophys. Res. Solid Earth* 119 (3), 2,138–2,152. <https://doi.org/10.1002/2013JB010719>.
- Rooney, T.O., 2017. The Cenozoic magmatism of East-Africa: Part I - Flood basalts and pulsed magmatism. *Lithos* 286–287, 264–301. <https://doi.org/10.1016/j.lithos.2017.05.014>.
- Ruegg, J.C., 1975. Main results about the crustal and upper mantle structure of the Djibouti region. In: *Afar Depression of Ethiopia: Proceedings of an International Symposium on the Afar Region and Related Rift Problems, Held in Bad Bergzabern, FR Germany, April 1–6, 1974*. Schweizerbart, Stuttgart, Germany, pp. 120–134.
- Stuart, G.W., Bastow, I.D., Ebinger, C.J., 2006. Crustal structure of the northern Main Ethiopian Rift from receiver function studies. *Geol. Soc. Spec. Publ.* 259, 253–267. <https://doi.org/10.1144/GSL.SP.2006.259.01.20>.
- Tesfaye, S., Harding, D.J., Kusky, T.M., 2003. Early continental breakup boundary and migration of the Afar triple junction, Ethiopia. *Geol. Soc. Am. Bull.* 115 (9), 1,053–1,067. <https://doi.org/10.1130/B25149.1>.
- Vigny, C., Huchon, P., Ruegg, J.-C., Khanbari, K., Asfaw, L.M., 2006. Confirmation of Arabia plate slow motion by new GPS data in Yemen. *J. Geophys. Res. Solid Earth* 111 (2), B02402. <https://doi.org/10.1029/2004JB003229>.
- Voss, M., Jokat, W., 2007. Continental-ocean transition and voluminous magmatic underplating derived from P-wave velocity modelling of the East Greenland continental margin. *Geophys. J. Int.* 170 (2), 580–604. <https://doi.org/10.1111/j.1365-246X.2007.03438.x>.
- Wang, T., Gao, S.S., Dai, Y., Yang, Q., Liu, K.H., 2019. Lithospheric structure and evolution of southern Africa: Constraints from joint inversion of Rayleigh wave dispersion and receiver functions. *Geochem. Geophys. Geosyst.* 20 (7), 3,311–3,327. <https://doi.org/10.1029/2019GC008259>.
- Watanabe, T., 1993. Effects of water and melt on seismic velocities and their application to characterization of seismic reflectors. *Geophys. Res. Lett.* 20 (24), 2,933–2,936. <https://doi.org/10.1029/93GL03170>.
- Whaler, K.A., Hautot, S., 2006. The electrical resistivity structure of the crust beneath the northern Main Ethiopian Rift. *Geol. Soc. Spec. Publ.* 259 (1), 293–305. <https://doi.org/10.1144/GSL.SP.2006.259.01.22>.
- WoldeGabriel, G., Aronson, J.L., Walter, R.C., 1990. Geology, geochronology, and rift basin development in the central sector of the Main Ethiopia Rift. *Geol. Soc. Am. Bull.* 102 (4), 439–458. [https://doi.org/10.1130/0016-7606\(1990\)102<0439:GGARBD>2.3.CO;2](https://doi.org/10.1130/0016-7606(1990)102<0439:GGARBD>2.3.CO;2).
- Wolfenden, E., Ebinger, C., Yirgu, G., Deino, A., Ayalew, D., 2004. Evolution of the northern Main Ethiopian Rift: Birth of a triple junction. *Earth Planet. Sci. Lett.* 224 (1–2), 213–228. <https://doi.org/10.1016/j.epsl.2004.04.022>.
- Wolfenden, E., Ebinger, C., Yirgu, G., Renne, P.R., Kelley, S.P., 2005. Evolution of a volcanic rifted margin: Southern Red Sea, Ethiopia. *Geol. Soc. Am. Bull.* 117 (7–8), 846–864. <https://doi.org/10.1130/B25516.1>.
- Yeck, W.L., Sheehan, A.F., Schulte-Pelkum, V., 2013. Sequential H-k Stacking to Obtain Accurate Crustal Thickness beneath Sedimentary Basins. *Bull. Seismol. Soc. Am.* 103 (3), 2,142–2,150. <https://doi.org/10.1785/0120120290>.
- Yu, Y., Song, J., Liu, K.H., Gao, S.S., 2015. Determining crustal structure beneath seismic stations overlying a low-velocity sedimentary layer using receiver functions. *J. Geophys. Res. Solid Earth* 120 (5), 3,208–3,218. <https://doi.org/10.1002/2014JB011610>.
- Zelt, B.C., Ellis, R.M., 1999. Receiver-function studies in the Trans-Hudson orogen, Saskatchewan. *Can. J. Earth Sci.* 36 (4), 585–603. <https://doi.org/10.1139/e98-109>.
- Zhu, L., Kanamori, H., 2000. Moho depth variation in southern California from teleseismic receiver functions. *J. Geophys. Res. Solid Earth* 105 (B2), 2,969–2,980. <https://doi.org/10.1029/1999JB900322>.